ACS APPLIED MATERIALS & INTERFACES

www.acsami.org

Research Article

High-Efficiency Gold Recovery Using Cucurbit[6]uril

Huang Wu, Leighton O. Jones, Yu Wang, Dengke Shen, Zhichang Liu, Long Zhang, Kang Cai, Yang Jiao, Charlotte L. Stern, George C. Schatz, and J. Fraser Stoddart*

Cite This: https://dx.doi.org/10.1021/acsami.0c09673

Read Online

ACCESS | Metrics & More | Article Recommendations | Supporting Information

ABSTRACT: Developing an extremely efficient and highly selective process for gold recovery is urgently desired for maintaining a sustainable ecological environment. Herein, we report a highly efficient gold-recovery protocol on the basis of the instantaneous assembly between cucurbit[6]uril (CB[6]) and $[AuX_4]^-$ (X = Cl/Br) anions. Upon mixing CB[6] with the four gold-bearing salts $MAuX_4$ (M = H/K, X = Cl/Br) in aqueous solutions, yellow or brown coprecipitates form immediately, as a result of multiple weak [Au−X···H−C] (X = Cl/Br) hydrogen-bonding and [Au−X···C=O] (X = Cl/Br) ion-dipole interactions. The gold-recovery efficiency, based on **CB[6]·HAuCl$_4$** coprecipitation, reaches 99.2% under optimized conditions. In the X-ray crystal superstructures, $[AuCl_4]^-$ anions and CB[6] molecules adopt an alternating arrangement to form doubly connected supramolecular polymers, while $[AuBr_4]^-$ anions are accommodated in the lattice between two-dimensional layered nanostructures composed of CB[6] molecules. DFT calculations have revealed that the binding energy (34.8 kcal mol^{-1}) between CB[6] molecules and $[AuCl_4]^-$ anions is higher than that (11.3−31.3 kcal mol^{-1}) between CB[6] molecules and $[AuBr_4]^-$ anions, leading to improved crystallinity and higher yields of **CB[6]·MAuCl$_4$** (M = H/K) coprecipitates. Additionally, a laboratory-scale gold-recovery protocol, aligned with an attractive strategy for the practical recovery of gold, was established based on the highly efficient coprecipitation of **CB[6]·HAuCl$_4$**. The use of CB[6] as a gold extractant provides us with a new opportunity to develop more efficient processes for gold recovery.

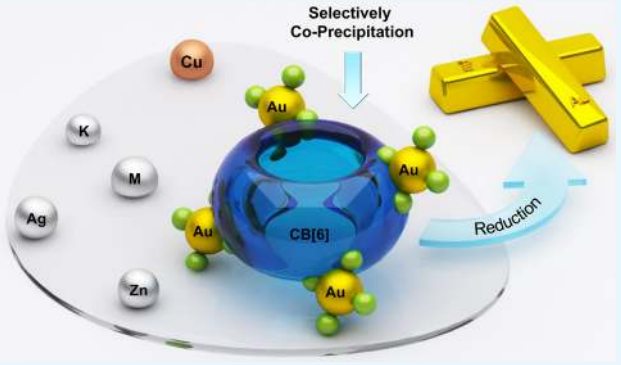

KEYWORDS: *coprecipitate, outer surface interaction, precious metal, resource recovery, solid-state superstructure, supramolecular assembly*

INTRODUCTION

We live in a time that could be called the electronic age. Most electronic appliances have a relatively short lifetime and are constantly being discarded either because they have reached the end of their useful lives or because a more attractive next-generation product has come on the market. The disposal of electronic waste (e-waste) draws more and more attention in the developed as well as in developing countries.[1−3] If not handled wisely, the toxic composition of this waste becomes hazardous to the environment and to the well-being of humankind. This e-waste, however, can become a valuable resource, since it contains[4] many noble metals and other useful materials. Hence, electronic waste, as a component of municipal solid waste, needs to undergo one or more of the 3Rs—reuse, recycle, and recover—on the grounds of environmental protection and resource recovery.[5] Gold, on account of its good electrical conductivity, high stability, and excellent malleability, plays[6,7] an indispensable role in today's electronics industry. About 288 metric tons of gold was utilized in electronics manufacture in 2018, accounting for 9% of the annual mine production of gold from all around the world.[8] Hence, the recovery of gold from e-waste is important from an economic as well as an environmental perspective. Many alternative methods have been developed to achieve gold recovery.[9−11] These methods include the leaching of gold-bearing e-waste and gold ore with a combination of *N*-bromosuccinimide and pyridine,[12] as well as the adsorption of ionic Au complexes with L-methionine-modified metal−organic frameworks[13] and amyloid-like protein membranes.[14] Meanwhile, developing a sustainable gold-recovery process that focuses on increasing gold-recovery efficiency and selectivity is mandatory.

In addition, noncovalent bonding strategies based on macrocyclic compounds, i.e., cyclodextrins,[15] crown ethers,[16,17] calixarenes,[18] pillararenes,[19] and so on, on account of their generally (i) associated mild reaction conditions, (ii) outstanding reversibility, and (iii) good selectivity, have been developed for the recognition of metal cationic complexes,

Received: May 27, 2020
Accepted: July 10, 2020
Published: July 10, 2020

including those containing Ni,[20] Rh,[21] Ag,[22] and Pt,[23] as well as anions, such as Cl^-,[24] $[SCN]^-$,[25] $[NO_3]^-$,[26] $[ClO_4]^-$,[27] $[H_2PO_4]^-$,[28] $[ReO_4]^-$,[29] and others.[30−32] Reports relating to the recognition and separation of Au complexes with macrocyclic compounds, however, are still somewhat limited. The first example[33,34] of the selective separation of an Au complex, discovered serendipitously in our laboratory, involves the alternating arrangement of $[K(OH_2)_6]^+/[AuBr_4]^-$ ion pair components inside the cavity of α-cyclodextrins (α-CDs), which assemble in a head-to-head/tail-to-tail manner to form a one-dimensional supramolecular complex facilitated by second-sphere coordination.

Recently, Tao et al.[35] reported that $[AuCl_4]^-$ anions could be imprisoned inside two slightly different supramolecular frameworks composed of cucurbit[8]uril (CB[8]). These authors also demonstrated[36] the selective recovery and detection of $[AuCl_4]^-$ with smaller cucurbit[*n*]urils (*n* = 5−7) based on outer-surface interactions. At one and the same time, we have finished, quite independently, our own research program on gold recovery using cucurbit[6]uril (CB[6]). We discovered serendipitously that CB[6]—one of the easiest members of this family to make and isolate as a pure compound[37−39]—is considerably more efficient than CB[8] when it comes to producing crystalline complexes or coprecipitates very quickly on the addition of $[AuX_4]^-$ (X = Cl/Br) anions. The partial negatively charged nature of the portals of carbonyl oxygen, along with its hydrophobic cavity, has made CB[6] attractive for complexing alkali,[40,41] alkaline earth,[37] transition,[42] and rare earth[43] metal cations, as well as organic ammonium.[39,44] Although CB[6] has been utilized widely in the fields of gas sorption[45,46] and drug delivery,[47,48] in addition to its incorporation into functional materials[49,50] and catalysts,[51,52] there are relatively few reports in the literature,[53,54] which exploit the outer-surface interactions of CB[6]. Herein, we present our findings relating to the trapping of both $[AuCl_4]^-$ and $[AuBr_4]^-$ anions as their acids and potassium salts with CB[6] facilitated by multiple weak [Au−X···H−C] (X = Cl/Br) hydrogen-bonding and [Au−X···C=O] (X = Cl/Br) ion-dipole interactions. After optimizing with respect to a wide range of experimental conditions, e.g., the relative concentrations of CB[6], $MAuX_4$ (M = H/K, X = Cl/Br) salts, and acid (HCl), we have achieved a gold-recovery efficiency of 99.2% based on the coprecipitation of CB[6] and $HAuCl_4$. Additionally, a laboratory-scale gold-recovery protocol, based on the highly efficient coprecipitation of the **CB[6]·HAuCl$_4$** adduct, has been demonstrated. This result indicates that CB[6] is a feasible gold extractant.

RESULTS AND DISCUSSION

Formation of Coprecipitates. Upon mixing any particular aqueous solution of $MAuX_4$ (M = H/K, X = Cl/Br, 20.0 mM, 0.6 mL) with an aqueous solution of CB[6] (8.0 mM, 1.5 mL) containing HCl (3.0 M) or HBr (3.5 M) at room temperature, yellow or brown coprecipitates form immediately. See Figure 1 and Supplementary Movie 1. This observation establishes the fact that the $[AuX_4]^-$ (X = Cl/Br) anions can form coprecipitates with CB[6] either in the presence or absence of K^+ ions, indicating that gold halide $[AuX_4]^-$ anions play a crucial role in the formation of the coprecipitates. Centrifugal filtration and air drying of the coprecipitates permitted isolation of the four complexes—which are identified by the descriptors **CB[6]·HAuCl$_4$**, **CB[6]·KAuCl$_4$**, **CB[6]·HAuBr$_4$**, and **CB[6]·KAuBr$_4$**—in bulk as either yellow or brown coprecipitates.

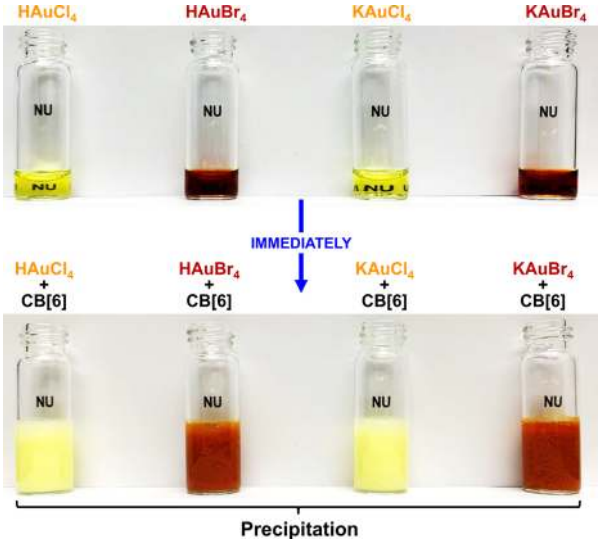

Figure 1. Formation of coprecipitates of **CB[6]·MAuX$_4$** (M = H/K, X = Cl/Br) from CB[6] and $MAuX_4$. When CB[6] (8 mM, 1.5 mL) in an aqueous HCl (3 M) or HBr (3.5 M) solution is added to aqueous solutions of $MAuX_4$ (20 mM, 0.6 mL), yellow or brown coprecipitates, respectively, are formed immediately. See Supplementary Movie 1.

The Fourier transform infrared (FTIR) spectra of all four coprecipitates show (Figure S7) a sharp vibrational band at ∼1728 cm^{-1}, characteristic of the stretching vibration of the CB[6] carbonyl (C=O) groups. Additionally, broad vibration bands observed at ∼1602, 1610, 1611, and 1606 cm^{-1} correspond, respectively, to the **CB[6]·HAuCl$_4$**, **CB[6]·KAuCl$_4$**, **CB[6]·HAuBr$_4$**, and **CB[6]·KAuBr$_4$** precipitates. These spectroscopic results provide qualitative evidence for the formation of the adducts. In order to quantify gold-recovery efficiencies based on the coprecipitates, all four filtrates were diluted and subjected to inductively coupled plasma optical emission spectroscopy (ICP-OES) analysis to determine the concentrations of remaining $[AuX_4]^-$ anions. On the basis of the initial and residual concentrations of $[AuX_4]^-$ in the aqueous solutions, the yields of precipitated $[AuX_4]^-$ can be obtained by calculation. The results revealed (Figure 2 and Table S6) that gold-recovery yields for all the

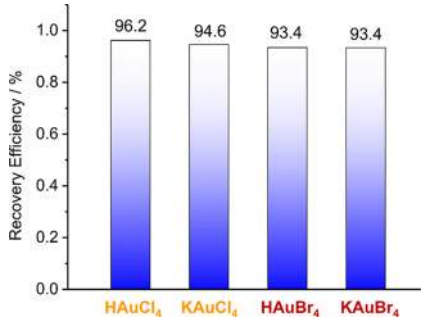

Figure 2. Gold-recovery efficiencies based on the coprecipitates from four aqueous solutions of CB[6] (5.7 mM) and $MAuX_4$ (5.7 mM) (M = H/K, X = Cl/Br), calculated according to the initial and residual concentrations of $[AuX_4]^-$ anions in the aqueous solutions which were measured at 25 °C by ICP-OES analysis.

https://dx.doi.org/10.1021/acsami.0c09673
ACS Appl. Mater. Interfaces XXXX, XXX, XXX−XXX

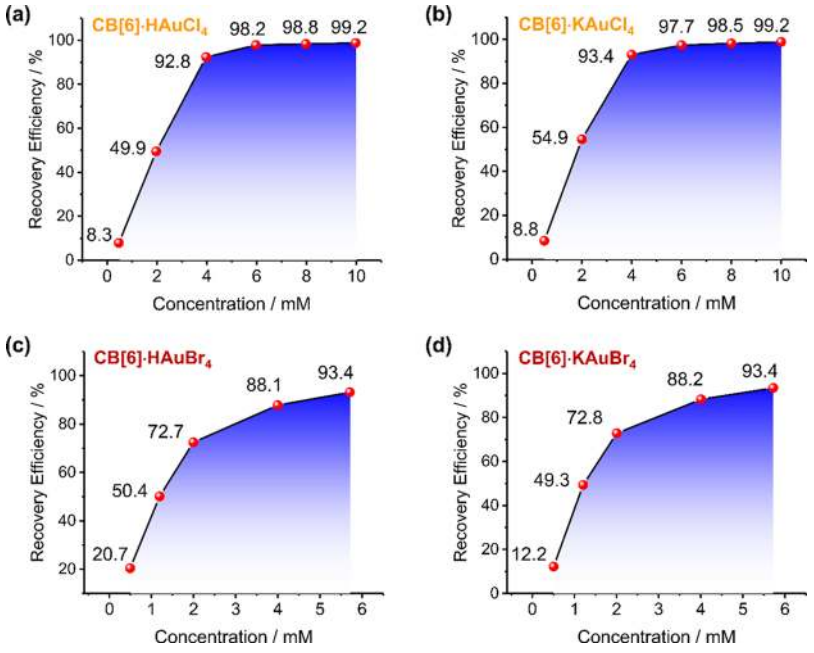

Figure 3. Effect of changes in the concentration of CB[6] and $MAuX_4$ (M = H/K, X = Cl/Br) on gold-recovery efficiency from the four coprecipitated adducts (a) **CB[6]·HAuCl$_4$**, (b) **CB[6]·KAuCl$_4$**, (c) **CB[6]·HAuBr$_4$**, and (d) **CB[6]·KAuBr$_4$**. The concentration of HCl is 2 M in all aqueous solutions of **CB[6]·MAuCl$_4$**, while the concentration of HBr is 2.5 M in all aqueous solutions of **CB[6]·MAuBr$_4$**.

combinations between CB[6] and $MAuX_4$ (M = H/K, X = Cl/Br) are in excess of 90.0% at concentrations of 5.7 mM. This yield is higher than that (78%) in our previous report[34] of the coprecipitate formed between α-CD and $KAuBr_4$. $HAuCl_4$ affords an even higher gold-recovery yield (96.2%), compared with that for $KAuCl_4$ (94.6%). By contrast, both $HAuBr_4$ and $KAuBr_4$ give the lowest gold-recovery yields of only 93.4%. These observations demonstrate that the nature of the $[AuX_4]^-$ anion influences the yield of the coprecipitate.

Optimizing Gold Recovery. Given the potential applications of CB[6] as a gold extractant, the yields of the **CB[6]·MAuX$_4$** coprecipitates were optimized with respect to the concentrations of CB[6] and $MAuX_4$. Different concentrations (0.5, 2.0, 4.0, 6.0, 8.0, and 10.0 mM) of $MAuCl_4$ (M = H/K) were prepared by dissolving $MAuCl_4$ salts in aqueous HCl (2.0 M) solutions. Upon addition of equimolar amounts of an aqueous CB[6] solution containing HCl (2.0 M) to the prepared aqueous $MAuCl_4$ solutions, yellow coprecipitates formed immediately. These coprecipitates were filtered immediately (<5 s), and the concentration of $[AuCl_4]^-$ remaining in the filtrates was analyzed by ICP-OES analysis. The results reveal (Figure 3a and Table S7) that the gold-recovery efficiencies, based on the **CB[6]·HAuCl$_4$** coprecipitate, change dramatically from 8.3 to 92.8% upon increasing the concentration of **CB[6]·HAuCl$_4$** from 0.5 to 4.0 mM in aqueous HCl solution. When the concentration of **CB[6]·HAuCl$_4$** was increased gradually to 10.0 mM, the yield of the coprecipitates reached 99.2% in aqueous HCl solution. Gold-recovery efficiencies, based on the **CB[6]·KAuCl$_4$** coprecipitate, were (Figure 3b and Table S8) analogous to those for **CB[6]·HAuCl$_4$** at different concentrations and, once again, increased with the increasing concentration of the adduct. These observations suggest that the higher the initial concentrations of the CB[6] and $MAuCl_4$, the higher will be the gold-recovery efficiency.

By contrast, when equimolar amounts of CB[6] in aqueous HBr (2.5 M) solution were added to the different concentrations (0.5, 1.2, 2.0, 4.0, and 5.7 mM) of $MAuBr_4$ (M = H/K) aqueous solution, gold-recovery efficiency, based on the **CB[6]·HAuBr$_4$** and **CB[6]·KAuBr$_4$** coprecipitates, increased from 20.7 to 93.4% (Figure 3c and Table S9) and 12.2 to 93.4% (Figure 3d and Table S10), respectively. The limited solubility of CB[6] in aqueous HBr solution, however, hampers a further increase in the initial concentration of CB[6] and $MAuBr_4$, limiting gold-recovery efficiency, based on **CB[6]·MAuBr$_4$** coprecipitation, to 93.4%. On the basis of the results relating to gold-recovery efficiencies with varying concentrations of CB[6] and $MAuX_4$, it can be concluded that higher initial concentrations of CB[6] and $MAuX_4$ will lead to higher gold-recovery efficiencies. On account of the higher solubility of CB[6] in aqueous HCl than in aqueous HBr, the gold-recovery efficiencies for the **CB[6]·MAuCl$_4$** series are higher than those for the **CB[6]·MAuBr$_4$** series, indicating that the $[AuCl_4]^-$ anion is the better candidate when it comes to the quantitative recovery of gold.

Taking into account the fact that the concentration of acid in gold-bearing solutions may vary in practice, gold-recovery efficiencies based on the **CB[6]·MAuCl$_4$** coprecipitates have been optimized with respect to the concentration of HCl. Six aqueous solutions of $MAuCl_4$ (6.0 mM), corresponding to HCl concentrations of 1.0, 2.0, 4.0, 6.0, 8.0, and 10.0 M, were prepared. Upon the addition of equimolar amounts of CB[6], the mixtures with 1.0 and 2.0 M HCl were found to generate copious amounts of coprecipitate, while the mixtures with 4.0 and 6.0 M HCl resulted in smaller amounts of coprecipitates. By contrast, no obvious coprecipitation occurred in the mixtures with 8.0 and 10.0 M HCl. It should be mentioned that CB[6] could not be dissolved completely in 1.0 M HCl aqueous solution. All of the coprecipitates were removed by filtration, and the concentrations of $[AuCl_4]^-$ remaining in the filtrates were measured by ICP-OES analysis. Gold-recovery

https://dx.doi.org/10.1021/acsami.0c09673
ACS Appl. Mater. Interfaces XXXX, XXX, XXX−XXX

efficiencies, based on the coprecipitates at different concentrations of HCl, were calculated according to the initial and residual concentrations of the $[AuCl_4]^-$ anion in the aqueous HCl solutions.

The results reveal (Figure 4a and Table S11) that the mixture with 2.0 M HCl affords the highest gold-recovery

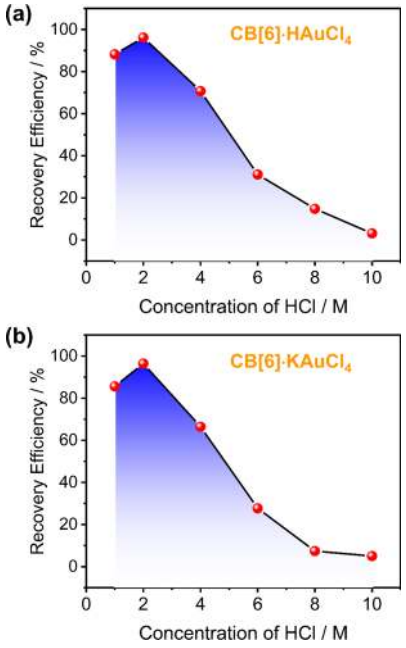

Figure 4. Effect of changes in the concentration of HCl on gold-recovery efficiency from two coprecipitated adducts (a) **CB[6]·HAuCl$_4$** and (b) **CB[6]·KAuCl$_4$**. The concentrations of CB[6] and $MAuCl_4$ in all aqueous solutions are 6 mM.

efficiency of 96.4%, while the efficiency for the mixture with 1.0 M HCl is 88.4%. This observation may be a consequence of the lower solubility of CB[6] in aqueous 1.0 M HCl, leading to the actual concentration of CB[6] being lower than 6.0 mM. When the concentration of HCl was changed from 2.0 to 10.0 M, gold-recovery efficiencies, based on the **CB[6]·HAuCl$_4$** coprecipitates, decreased from 96.4 to 3.3%. These results indicate that higher concentrations of HCl lead to higher solubilities of the **CB[6]·HAuCl$_4$** adducts and lower gold-recovery efficiencies. In the case of **CB[6]·KAuCl$_4$**, gold-recovery efficiencies based on coprecipitates showed (Figure 4b and Table S12) a similar trend to those for **CB[6]·HAuCl$_4$**. Upon increasing the concentration of HCl from 1.0 to 10.0 M, the mixture with 2.0 M HCl exhibited the highest gold-recovery efficiency (96.9%). On basis of these profiles, it can be concluded that 2.0 M HCl solution constitutes the optimum solvent system for gold recovery. Gold-recovery efficiencies, based on the **CB[6]·MAuCl$_4$** coprecipitates, all show a downward trend on further increasing or decreasing the concentration of HCl.

X-ray Crystallographic Analysis of Solid-State Superstructures. In order to gain additional insight into the driving forces behind coprecipitate formation, we turned our attention to crystallization and single-crystal X-ray diffraction studies. High quality single crystals for all five adducts—namely, **CB[6]·HAuCl$_4$**, **CB[6]·KAuCl$_4$**, **CB[6]·HAuBr$_4$**, **CB[6]·KAuBr$_4$**, and **CB[6]·HAuCl$_{2.28}$Br$_{1.72}$**—suitable for X-ray crystallography were obtained by slow liquid–liquid diffusion. When an equimolar amount of aqueous $MAuX_4$ solution was layered carefully on top of an aqueous solution of CB[6] containing either HCl or HBr, high quality yellow or brown cocrystals, respectively, were obtained as a result of the slow diffusion of $MAuX_4$ and CB[6] molecules.

Solid-State Superstructures of the CB[6]·MAuCl$_4$ Adducts. The solid-state superstructure of **CB[6]·HAuCl$_4$** reveals (Figure 5 and Table S1) that the adduct adopts the

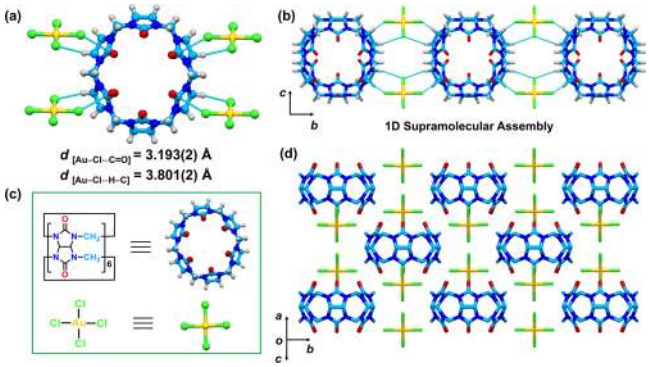

Figure 5. Solid-state superstructure of the adduct formed between CB[6] and $HAuCl_4$. (a) Ball-and-stick representation showing that every CB[6] molecule interacts with four $[AuCl_4]^-$ anions through [Au–Cl···H–C] hydrogen-bonding and ion-dipole interactions. (b) Supramolecular assembly of the one-dimensional nanostructure extending along the *b* axis in which adjacent CB[6] molecules are connected by two parallelly aligned $[AuCl_4]^-$ anions. (c) Structural formulas of CB[6] and $[AuCl_4]^-$ anions. (d) Solid-state superstructure of **CB[6]·HAuCl$_4$**, which is made up of the parallelly aligned 1D supramolecular assemblies illustrated in (b). The H_2O molecules are omitted for the sake of clarity. H: gray, C: pale blue, N: blue, O: red, Cl: green, and Au: yellow.

monoclinic space group *C*2/*m*, in contrast with that (*P*321 or $P\bar{3}ml$) obtained for CB[6]/$NaAuCl_4$ in a previous report.[55] Every CB[6] molecule interacts (Figure 5a) with four equivalent $[AuCl_4]^-$ anions through ion-dipole interactions and hydrogen bonding. It turns out that these noncovalent bonding interactions are the classic ones employed[56−59] in anion recognition. The [Au–Cl···C=O] ion-dipole interactions refer to the Cl atoms in $[AuCl_4]^-$ and the carbonyl carbon atoms on CB[6], which interact at a distance of 3.193(2) Å. The hydrogen-bond distance in [Au–Cl···H–C] involving the Cl atoms in $[AuCl_4]^-$ and the electrostatically positive methine hydrogen atoms on the outer surface of CB[6] is 3.801(2) Å. On the other hand, every CB[6] is surrounded (Figure 7b) by another six CB[6] molecules, wherein (i) four of them are sustained by hydrogen-bonding and dipole-dipole interactions between the electron-rich carbonyl oxygen atoms on CB[6] and the electron-poor methylene hydrogen and carbonyl carbon atoms on neighboring CB[6] molecules, with a distance of 3.154(2) Å (C=O···C), while (ii) the other two CB[6] molecules are held together by van der Waals interactions between two carbonyl carbon atoms located at a distance of 3.368(2) Å. Along the *b* axis, two adjacent CB[6] molecules are observed (Figure 5b) to be held together by two parallelly aligned $[AuCl_4]^-$ anions at a distance of 9.17 Å (Au···Au). Only three of the Cl atoms in $[AuCl_4]^-$ exhibit, by means of [Au–Cl···H–C] and [Au–Cl···C=O] interactions, noncovalent bonding with adjacent CB[6] moieties. Accordingly, CB[6] molecules and $[AuCl_4]^-$ anions adopt an alternating arrangement along the *b* axis, forming (Figure 5b) doubly connected one-dimensional (1D) supra-

https://dx.doi.org/10.1021/acsami.0c09673
ACS Appl. Mater. Interfaces XXXX, XXX, XXX−XXX

molecular polymers. Bundles of these nanostructures are then packed tightly by means of hydrogen-bonding and van der Waals interactions between contiguous CB[6] molecules to form (Figure 5d) a well-ordered array that constitutes the single crystal. Upon layering carefully the solution of $KAuCl_4$ on top of an aqueous CB[6] solution, high quality yellow cocrystals were obtained after approximately 12 h. X-ray crystallography revealed that CB[6] and $[AuCl_4]^-$ are also arranged in an alternating manner, forming 1D doubly connected supramolecular polymers (Figure S1), wherein the $[AuCl_4]^-$ anions act as linkers between two adjacent CB[6] molecules along the *b* axis by means of [Au−Cl···H−C] hydrogen-bonding and [Au−Cl···C═O] interactions. Notably, K^+ ions are absent in the crystalline lattice. Presumably, they are present in the mother liquors. This phenomenon indicates that CB[6] crystallizes selectively with $[AuCl_4]^-$ anions without interference from K^+ ions. The example of CB[6] interacting preferentially with anions rather than with cations is rare, since the portal-region carbonyl oxygen atoms in cucurbiturils show generally strong affinities for metal and organic cations according to many reports[60,61] in the literature. Possible reasons for the selective crystallization between CB[6] molecules and $[AuCl_4]^-$ anions include (i) replacement of K^+ ions by protons in aqueous acidic solution during the crystallization process and (ii) the highly crystalline nature of the **CB[6]·[AuCl$_4$]$^-$** adducts. These observations, which point to the fact that $[AuCl_4]^-$ captured by CB[6] to form **CB[6]·MAuCl$_4$** adducts is a selective process, even in the presence of other metal counter-cations, augur well for developing selective gold-recovery protocols for the separation of gold from complex mixtures of metal salts.

Solid-State Superstructures of the CB[6]·MAuBr$_4$ Adducts. Although the $[AuBr_4]^-$ anion possesses a square-planar geometry, similar to that of $[AuCl_4]^-$, the solid-state superstructure of **CB[6]·HAuBr$_4$** is quite different from that of **CB[6]·HAuCl$_4$**, in that **CB[6]·HAuBr$_4$** adopts (Figure 6 and Table S1) the tetragonal space group $I\bar{4}2d$. A detailed superstructure analysis shows (Figure 6a) that, in the presence of water molecules, CB[6] macrocycles form a 2D layered superstructure in the *a*-*b* plane. The water molecules are disordered and surrounded by four CB[6] molecules, courtesy of a [C═O···H−O] hydrogen-bonding motif with a distance of 2.896(8) Å. In the 2D layered nanostructure, CB[6] molecules are located perpendicular to the *a*-*b* plane and interact with another four CB[6] molecules sustained (Figure 7e) by multiple [C═O···H−C] hydrogen bonds and [C═O··· C] dipole−dipole interactions with distances from 2.94(1) to 3.44(1) Å. The 2D layered nanostructure is observed (Figure 6b) to be held together by $[AuBr_4]^-$ anions, relying on hydrogen-bonding and ion-dipole interactions to form well-ordered arrays along the *c* axis. The $[AuBr_4]^-$ anions exhibit two different bonding modes with CB[6] molecules, which will be identified by the descriptors α-$[AuBr_4]^-$ and β-$[AuBr_4]^-$, i.e., they are polymorphs. The α-$[AuBr_4]^-$ anion is related by a 42.8° dihedral angle about the *a*-*b* plane and is connected (Figure 6c) with two CB[6] molecules located in adjacent layers as a result of [Au−Br···H−C] interactions, with distances ranging from 3.67(1) to 3.90(1) Å. The disordered β-$[AuBr_4]^-$ anion adopts a parallel arrangement (Figure 6d) in the *a*-*b* plane and interacts with five CB[6] molecules by means of the [Au−Br···H−C] hydrogen-bonding and [Au− Br···C═O] interactions, with distances of 3.87(1)−3.91(2) and 3.31(1)−3.53(1) Å, respectively.

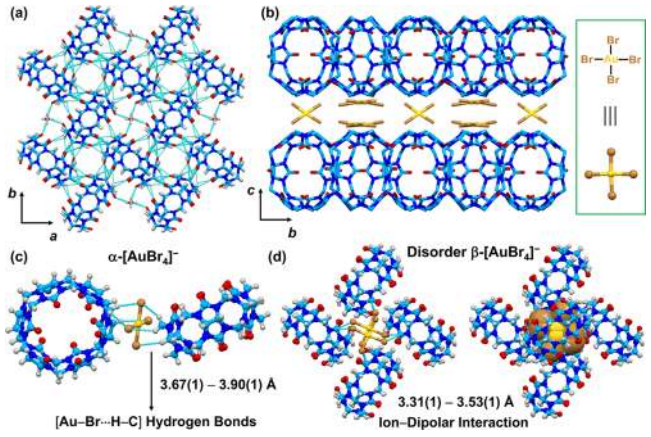

Figure 6. Solid-state superstructure of the adduct formed between CB[6] and $HAuBr_4$. (a) Supramolecular assembly of the 2D nanostructure in the *a*-*b* plane as a result of multiple hydrogen bonds between H_2O and CB[6] molecules, as well as between two adjacent CB[6] molecules. (b) Solid-state superstructure of **CB[6]·HAuBr$_4$** in which two polymorphs of the $[AuBr_4]^-$—α-$[AuBr_4]^-$ and β-$[AuBr_4]^-$—anion are accommodated in the lattice between the 2D supramolecular assemblies illustrated in (a). (c) Ball-and-stick representation showing that every α-$[AuBr_4]^-$ anion interacts with two CB[6] molecules through [Au−Br···H−C] hydrogen bonds. (d) β-$[AuBr_4]^-$ anions interact with five CB[6] molecules, which are disordered over two positions with 50:50 occupancies. H: gray, C: pale blue, N: blue, O: red, Br: brown, and Au: yellow.

Notably, when an $HAuBr_4$ aqueous solution underwent diffusion into a CB[6] aqueous solution with HCl (3 M), brown single crystals were obtained after 12 h. X-ray crystallographic analysis reveals (Figure S3c) that 57% of the Br atoms have been exchanged with Cl ones. The solid-state superstructure (Figure S3) of the **CB[6]·HAuCl$_{2.28}$Br$_{1.72}$** adduct is quite different from that of **CB[6]·HAuBr$_4$**, which is isostructural with **CB[6]·HAuCl$_4$**. These results indicate that (i) **CB[6]·HAuCl$_{2.28}$Br$_{1.72}$** has high crystallinity, and (ii) the affinity between CB[6] molecules and $[AuCl_4]^-$ anions is larger than that between CB[6] molecules and $[AuBr_4]^-$ anions.

The **CB[6]·KAuBr$_4$** adduct crystallizes in the triclinic space group $P\bar{1}$ (Figure S2 and Table S1), which is different from that ($I\bar{4}2d$) associated with the **CB[6]·HAuBr$_4$** adduct. In the solid-state superstructure of **CB[6]·KAuBr$_4$**, the K^+ ions cocrystallize with the **CB[6]·[AuBr$_4$]$^-$** adduct in a molar ratio of 1:2, indicating that only half of the K^+ ions takes part in crystal formation. This situation differs from the solid-state superstructure of the **CB[6]·KAuCl$_4$** adduct in which K^+ ions are absent. A detailed solid-state superstructure analysis reveals that **CB[6]·KAuBr$_4$** expresses a similar assembly mode to **CB[6]·HAuBr$_4$**, although they reside in different space groups. In the solid-state superstructure of **CB[6]·KAuBr$_4$**, CB[6] molecules form (Figure S2a) 2D layers in the *a*-*b* plane, stabilized by [C═O···H−C] interactions between adjacent CB[6] molecules, as well as ion-dipole interactions involving K^+ ions and carbonyl oxygen atoms in CB[6], where the K^+−O distances are in the range of 2.77−2.82 Å. The $[AuBr_4]^-$ anions are also accommodated (Figure S2b) in the lattice between two layers, serving as linkers to facilitate well-ordered stacking in the 2D layered nanostructure. The $[AuBr_4]^-$ anions exhibit (Figure S2b) two different bonding modes with CB[6] in the solid-state superstructure of **CB[6]·KAuBr$_4$**. The α-$[AuBr_4]^-$ anion interacts (Figure S2c) with two CB[6]

https://dx.doi.org/10.1021/acsami.0c09673
ACS Appl. Mater. Interfaces XXXX, XXX, XXX−XXX

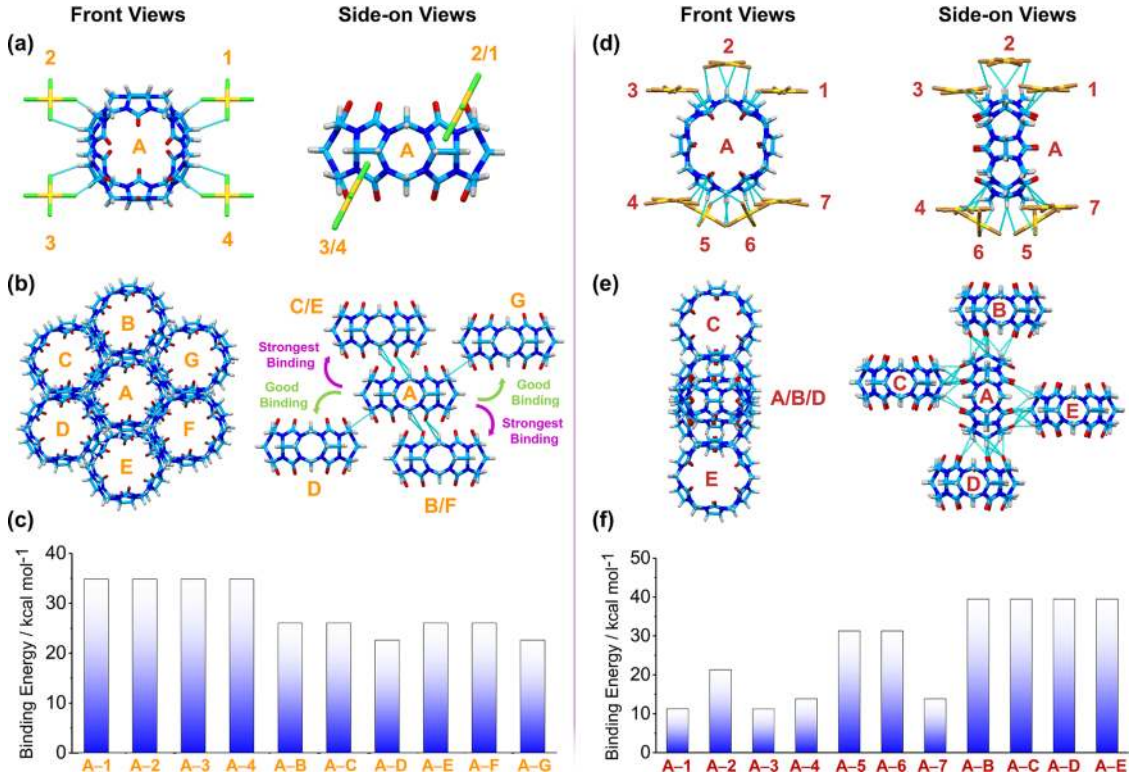

Figure 7. Solid-state superstructures and binding energies between CB[6] and $[AuX_4]^-$ (X = Cl/Br) anions obtained by DFT calculations. (a, b) Capped-stick representation illustrating the different views of how CB[6] (A) interacts with four $[AuCl_4]^-$ anions (1−4) and six adjacent CB[6] molecules (B−G) in the solid-state superstructures of **CB[6]·HAuCl$_4$**. (c) Results of DFT calculations of the binding energies between CB[6] (A) and four connected $[AuCl_4]^-$ anions (1−4) in addition to six adjacent CB[6] molecules (B−G). (d, e) Capped-stick representation illustrating different views of how CB[6] (A) interacts with seven $[AuBr_4]^-$ anion (1−7) and four adjacent CB[6] molecules (B−E) in the solid-state superstructures of **CB[6]·HAuBr$_4$**. (f) Results of DFT calculations on the binding energies between CB[6] (A) and seven connected $[AuBr_4]^-$ anions in addition to four adjacent CB[6] molecules (B−E). A−X (X = 1−7/B−G) representing the two interacting molecules defined in Figure 7. H: gray, C: pale blue, N: blue, O: red, Cl: green, Br: brown, and Au: yellow.

molecules in adjacent layers by means of [Au−Br···H−C] interactions with a distance of 3.97(2) Å. The β-$[AuBr_4]^-$ anion interacts (Figure S2d) with five CB[6] molecules involving the Br atoms of the $[AuBr_4]^-$ anions and one methylene hydrogen and four carbon atoms in the carbonyl groups with distances of 3.80(2) and 3.40(2)−3.43(2) Å, respectively. In contrast with $[AuBr_4]^-$ in the solid-state superstructure of **CB[6]·HAuBr$_4$**, the α-$[AuBr_4]^-$ anions in **CB[6]·KAuBr$_4$** are disordered (Figure S2) over two positions with 50:50 occupancies, while the β-$[AuBr_4]^-$ anions exhibit no disorder. When the solid-state superstructures of **CB[6]·HAuBr$_4$** and **CB[6]·KAuBr$_4$** are compared, it becomes evident that (i) the H_2O molecules in the 2D layered superstructure are replaced by K^+ ions, and (ii) the bonding mode between CB[6] molecules and $[AuBr_4]^-$ anions is different.

Outer Surface Host−Guest Interactions. The solid-state superstructures of the five adducts formed between CB[6] and $MAuX_4$ (M = H/K, X = Cl/Br) lead us to the conclusion that (i) both $[AuCl_4]^-$ and $[AuBr_4]^-$ anions are accommodated outside rather than inside the cavities of CB[6], aided and abetted by weak hydrogen-bonding and ion-dipole interactions between halogen atoms and the (a) methine, (b) bridged methylene hydrogen, and (c) carbonyl carbon atoms on the outer surface of CB[6], (ii) K^+ ions contribute insignificantly to the formation and stabilization of the superstructure, and (iii) although the $[AuCl_4]^-$ anion has a similar square-planar geometry to the $[AuBr_4]^-$ anion, the solid-state superstructures of the **CB[6]·HAuCl$_4$** adducts are entirely different from those of **CB[6]·HAuBr$_4$**.

Characterization by PXRD and TGA. In order to investigate the crystallinity and stability of the four coprecipitates, **CB[6]·HAuCl$_4$**, **CB[6]·KAuCl$_4$**, **CB[6]·HAuBr$_4$**, and **CB[6]·KAuBr$_4$**, powder X-ray diffraction (PXRD) and thermogravimetric analyses (TGA) were carried out. Upon mixing equimolar amounts of CB[6] and $MAuX_4$ in aqueous solution with either HCl (2 M) or HBr (2.5 M), yellow or brown suspensions formed immediately. All the suspended solids, which settled at the bottom of the vials after 1 h, were subjected to powder XRD analysis after removing the supernatant. The experimental PXRD patterns of **CB[6]·MAuCl$_4$** (M = H/K) matched (Figure S4a,b) well with the simulated patterns based on the single-crystal X-ray data, indicating that the microstructures of the **CB[6]·MAuCl$_4$** coprecipitates are consistent with those of the crystal superstructures. By contrast, the experimental PXRD patterns of **CB[6]·MAuBr$_4$** (M = H/K) show (Figure S4c,d) some broad diffraction peaks, an observation that suggests that the coprecipitate of **CB[6]·MAuBr$_4$** possesses a weak tendency to crystallize. Interestingly, the coprecipitates of **CB[6]·MAuCl$_4$** transformed (Figure S5) spontaneously into large crystals, visible to the naked eye, after standing for 3 days, while the coprecipitates of **CB[6]·MAuBr$_4$** showed no obvious changes. This phenomenon demonstrates the fact that coprecipitates of **CB[6]·MAuCl$_4$** undergo an Ostwald ripening process.[62,63] The

https://dx.doi.org/10.1021/acsami.0c09673
ACS Appl. Mater. Interfaces XXXX, XXX, XXX−XXX

PXRD patterns for the large crystals (Figure S6) of **CB[6]·MAuCl$_4$** are identical to those of the initial coprecipitates, indicating that no crystalline transformation occurred during Ostwald ripening. Based on the PXRD analysis of the four adducts, it can be concluded that the coprecipitate of **CB[6]·MAuCl$_4$** is easier to crystallize than that of **CB[6]·MAuBr$_4$**. TGA profiles (Figure S8) for **CB[6]·HAuX$_4$** (X = Cl/Br) are similar to those for **CB[6]·KAuX$_4$** over the entire temperature range of 35 to 800 °C, whereas the adducts with or without K^+ ions possess thermostability up to 200 °C. The **CB[6]·MAuCl$_4$** and **CB[6]·MAuBr$_4$** begin to suffer loss of mass at temperatures around 225 and 200 °C, respectively, owing most likely to halide release. The most significant decompositions occurred around 385 and 345 °C for the **CB[6]·MAuCl$_4$** and **CB[6]·MAuBr$_4$** adducts, respectively, arising from the breakdown of CB[6].[64] Finally, approximately 53 and 65 wt % of the original mass of the **CB[6]·MAuCl$_4$** and **CB[6]·MAuBr$_4$** adducts, respectively, were lost at 800 °C. Based on these results, it can be concluded that the decomposition temperatures for the **CB[6]·MAuCl$_4$** (M = H/K) adducts are higher than those for the corresponding **CB[6]·MAuBr$_4$**, suggesting that the supramolecular associations between CB[6] and $MAuCl_4$ have better thermostability than those between CB[6] and $MAuBr_4$.

DFT Calculations. In order to gain a better understanding of the different crystallization behaviors and the binding energy between CB[6] and $[AuX_4]^-$ (X = Cl/Br), DFT calculations were carried out based on the solid-state superstructures of the **CB[6]·HAuCl$_4$** and **CB[6]·HAuBr$_4$** adducts. X-ray crystallographic analysis of the **CB[6]·HAuCl$_4$** adduct indicates (Figure 7b) that the central CB[6] molecule is surrounded by six neighboring CB[6] molecules. Calculations reveal that the binding energy between the central CB[6] molecule and four identical CB[6] molecules, sustained by the [C═O···H−C] interactions, is 26.0 kcal mol^{-1}. This value is higher than that (22.6 kcal mol^{-1}) involving the other two CB[6] molecules, which are stabilized by van der Waals interactions (Figure 7c and Table S3). CB[6] also interacts (Figure 7a) with four equivalent $[AuCl_4]^-$ anions. The binding energy between CB[6] molecule and these anions is 34.8 kcal mol^{-1} (Figure 7cc and Table S2), which is higher than the largest binding energy (26.0 kcal mol^{-1}) between the two CB[6] molecules. Herein, most likely, lies the origin of why CB[6] interacts preferentially with $[AuCl_4]^-$ anions rather than self-aggregating during the crystallization and coprecipitation processes. X-ray crystallographic analysis of the **CB[6]·HAuBr$_4$** adduct indicates (Figure 7e) that every CB[6] molecule interacts with four adjacent CB[6] molecules. The binding energy between the two neighboring CB[6] is 39.5 kcal mol^{-1} (Figure 7f and Table S5). CB[6] is also surrounded (Figure 7d) by seven $[AuBr_4]^-$ anions stabilized by hydrogen-bonding and ion-dipole interactions. The calculated binding energy between CB[6] and $[AuBr_4]^-$ ranges from 11.3 to 31.3 kcal mol^{-1} (Figure 7f and Table S4). Apparently, the binding energy (39.5 kcal mol^{-1}) between two CB[6] molecules is much higher than that (11.3−31.3 kcal mol^{-1}) between CB[6] molecules and $[AuBr_4]^-$ anions, so that CB[6] prefers to form (Figure 6a) a 2D layered nanostructure with itself in the *a*-*b* plane. When comparing the binding energy between CB[6] molecules and $[AuCl_4]^-$ anions with that of CB[6] molecules and $[AuBr_4]^-$ anions, it can be seen (Figure 7c,f) that the binding energy (34.8 kcal mol^{-1}) of CB[6] to $[AuCl_4]^-$ is higher than that (11.3−31.3 kcal mol^{-1}) of CB[6] to $[AuBr_4]^-$. The bottom line is that the **CB[6]·MAuCl$_4$** adducts exhibit a higher degree of stability and crystallinity than **CB[6]·MAuBr$_4$**, indicating that the $[AuCl_4]^-$ anion is the better candidate when it comes to gold recovery.

Gold-Recovery Experiment. In an attempt to test the validity of employing CB[6] for gold recovery, a gold-bearing alloy wire was employed as a surrogate for gold-bearing scrap in the development of a laboratory-scale gold-recovery experiment according to the flow diagram illustrated in Figure 8. On account of the highest coprecipitation yield (99.2%) and excellent crystallization properties of the **CB[6]·HAuCl$_4$** adduct, $HAuCl_4$ was chosen as the target intermediate. A yellow gold-bearing alloy wire (30 mg), containing 58% wt of Au and 42% wt of Cu, Zn, and Ag, was etched by the minimum volume of a mixed solution of HCl and H_2O_2 to convert Au into $HAuCl_4$.[65,66] According to prior optimization experiments, the acid concentration of the $HAuCl_4$-containing solution was adjusted to 2 M. Insoluble AgCl impurities were removed by filtration. When an aqueous solution of CB[6] was added to the filtrate, the coprecipitation of **CB[6]·HAuCl$_4$** occurred immediately. This observation indicates that the relatively large amounts of Cu and Zn salts had a negligible impact on the coprecipitation process. Following filtration of the coprecipitates from the mixture, the **CB[6]·HAuCl$_4$** solid was dispersed in aqueous acid solution and reduced with $N_2H_4{\cdot}H_2O$. Finally, the gold metal was recovered by filtration. ICP-OES analysis reveals (Tables S13, S14) that 99.8% of the gold present in the raw material was recovered, and its purity is 98.1%. In addition, any $HAuCl_4$ remaining in the filtrate can be recycled, while the CB[6] can be reused after recrystallization, improving significantly the utilization of reagents and decreasing the recovery costs. In order to demonstrate the applicability of employing CB[6] to recover smaller amounts of gold, two solutions of mixtures containing 5.5 and 2.6% wt of gold were prepared, and experiments were performed on them as described for the sample with 58% wt of gold. ICP-OES Analyses indicated (Table S15) that gold-recovery efficiencies are 98.5 and 97.4%, respectively. The results of these laboratory-scale gold-recovery experiments provide us with an opportunity to develop a highly efficient and feasible protocol for the recovery of gold on a larger scale.

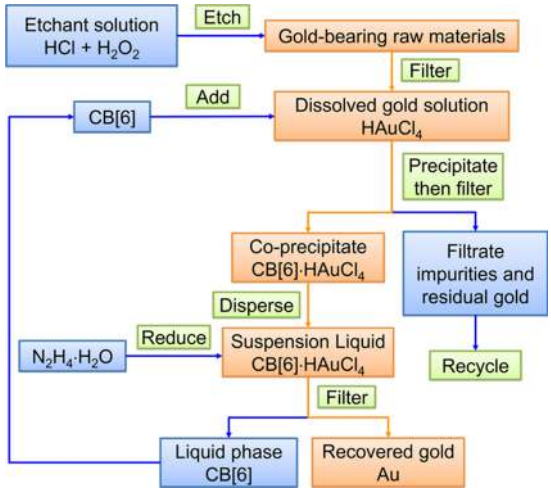

Figure 8. Gold-recovery flow diagram based on the coprecipitation of **CB[6]·HAuCl$_4$**. Light orange arrows and boxes indicate the flow direction for the recovery of gold.

https://dx.doi.org/10.1021/acsami.0c09673
ACS Appl. Mater. Interfaces XXXX, XXX, XXX−XXX

CONCLUSIONS

Instantaneous self-assembly of CB[6] molecules and $MAuX_4$ anions (M = H/K, X = Cl/Br) leads to rapid coprecipitation of **CB[6]·HAuCl$_4$**, **CB[6]·KAuCl$_4$**, **CB[6]·HAuBr$_4$**, and **CB[6]·KAuBr$_4$** adducts. This coprecipitation process is facilitated by weak hydrogen-bonding and ion-dipole interactions. During the systematic optimization of experimental conditions, we found that the higher the initial concentrations of CB[6] and $MAuX_4$, the higher is the gold-recovery efficiency. The **CB[6]·HAuCl$_4$** adduct affords the highest yield (99.2%) for gold recovery. The CB[6] and $[AuCl_4]^-$ moieties adopt an alternating arrangement in the crystal superstructure, while in the case of $[AuBr_4]^-$, the anions are accommodated in the lattice between the 2D layered nanostructures made up of CB[6], indicating that subtle changes in building blocks will lead to different superstructures and properties. Benefiting from the higher binding energy between CB[6] and $[AuCl_4]^-$ compared with that between CB[6] and $[AuBr_4]^-$, the **CB[6]·MAuCl$_4$** adducts show increased stability and crystallinity, compared with **CB[6]·MAuBr$_4$**. Finally, a laboratory-scale gold-recovery process was established based on the coprecipitation of **CB[6]·HAuCl$_4$** in which 99.8% of the gold present in the raw material has been recovered. Such a gold-recovery strategy leads to a fast and effective process with high recovery efficiency, thus demonstrating considerable potential for finding practical applications.

ASSOCIATED CONTENT

Supporting Information

The Supporting Information is available free of charge at https://pubs.acs.org/doi/10.1021/acsami.0c09673.

Detailed information regarding the experimental methods and procedures, X-ray crystallographic data, ICP-OES analysis, powder-XRD, Fourier-transform infrared spectroscopy, thermogravimetric analysis, and DFT calculations for the adducts, **CB[6]·HAuCl$_4$**, **CB[6]·KAuCl$_4$**, **CB[6]·HAuBr$_4$**, **CB[6]·KAuBr$_4$**, and **CB[6]·HAuCl$_{2.28}$Br$_{1.72}$** (PDF)

X-ray crystallographic data of the complex CB[6]·$HAuCl_4$ (CIF)

X-ray crystallographic data of the complex CB[6]·$KAuCl_4$ (CIF)

X-ray crystallographic data of the complex CB[6]·$HAuBr_4$ (CIF)

X-ray crystallographic data of the complex CB[6]·$KAuBr_4$ (CIF)

X-ray crystallographic data of the complex CB[6]·$HAuCl_{2.28}Br_{1.72}$ (CIF)

Formation of yellow or brown coprecipitates, as a result of multiple weak hydrogen-bonding and ion-dipole interactions, upon mixing CB[6] with the four gold-bearing salts $MAuX_4$ (M = H/K, X = Cl/Br) in aqueous solutions (MP4)

AUTHOR INFORMATION

Corresponding Author

J. Fraser Stoddart − *Department of Chemistry, Northwestern University, Evanston, Illinois 60208, United States; School of Chemistry, University of New South Wales, Sydney, New South Wales 2052, Australia; Institute for Molecular Design and Synthesis, Tianjin University, Tianjin 300072, P.R. China;* orcid.org/0000-0003-3161-3697; Phone: (+1) 847-491-3793; Email: stoddart@northwestern.edu

Authors

Huang Wu − *Department of Chemistry, Northwestern University, Evanston, Illinois 60208, United States;* orcid.org/0000-0002-7429-0982

Leighton O. Jones − *Department of Chemistry, Northwestern University, Evanston, Illinois 60208, United States;* orcid.org/0000-0001-6657-2632

Yu Wang − *Department of Chemistry, Northwestern University, Evanston, Illinois 60208, United States;* orcid.org/0000-0002-0085-3308

Dengke Shen − *Department of Chemistry, Northwestern University, Evanston, Illinois 60208, United States;* orcid.org/0000-0002-3251-2372

Zhichang Liu − *School of Science, Westlake University, Hangzhou 310024, China;* orcid.org/0000-0003-3412-512X

Long Zhang − *Department of Chemistry, Northwestern University, Evanston, Illinois 60208, United States*

Kang Cai − *Department of Chemistry, Northwestern University, Evanston, Illinois 60208, United States;* orcid.org/0000-0002-8883-0142

Yang Jiao − *Department of Chemistry, Northwestern University, Evanston, Illinois 60208, United States*

Charlotte L. Stern − *Department of Chemistry, Northwestern University, Evanston, Illinois 60208, United States*

George C. Schatz − *Department of Chemistry, Northwestern University, Evanston, Illinois 60208, United States;* orcid.org/0000-0001-5837-4740

Complete contact information is available at: https://pubs.acs.org/10.1021/acsami.0c09673

Author Contributions

H.W. conceived the research and carried out most of the experiments and analyses. L.O.J. and G.C.S. conducted the DFT calculations. Y.W. carried out the powder X-ray diffraction measurements. D.S. contributed to the design of the graphics illustrated in the figures. C.L.S. performed the X-ray crystallographic analyses. H.W. and Y.W. wrote the manuscript. Z.L., L.Z., K.C., and Y.J. participated in discussions and contributed to the preparation of the manuscript. J.F.S. directed and supervised the research as well as edited and re-edited the manuscript and Supporting Information. H.W., L.O.J., Z.L., and J.F.S. responded to the reviewer comments and contributed to the final presentation of the manuscript.

Notes

The authors declare no competing financial interest.

ACKNOWLEDGMENTS

This research work was funded by the Center for Sustainable Separations of Metals (CSSM), a National Science Foundation (NSF) Center for Chemical Innovation (CCI), grant number CHE-1925708. This research was also supported in part by the computational resources and staff contributions provided for the Quest High Performance Computing Facility at Northwestern University, which is jointly supported by the Office of the Provost, the Office for Research, and Northwestern University Information Technology. Z.L. acknowledges support from the National Natural Science Foundation of China (No. 21971211) and the Supercomputer Center of Westlake

https://dx.doi.org/10.1021/acsami.0c09673
ACS Appl. Mater. Interfaces XXXX, XXX, XXX−XXX

University. We wish to thank Dr. Margaret E. Schott for help with editing.

REFERENCES

(1) Ogunseitan, O. A.; Schoenung, J. M.; Saphores, J. D.; Shapiro, A. A. The Electronics Revolution: From E-Wonderland to E-Wasteland. *Science* **2009**, *326*, 670−671.

(2) Wang, Z.; Zhang, B.; Guan, D. Take Responsibility for Electronic-Waste Disposal. *Nature* **2016**, *536*, 23−25.

(3) Kannan, D.; Govindan, K.; Shankar, M. India: Formalize Recycling of Electronic Waste. *Nature* **2016**, *530*, 281.

(4) Ilankoon, I.; Ghorbani, Y.; Chong, M. N.; Herath, G.; Moyo, T.; Petersen, J. E-Waste in the International Context−A Review of Trade Flows, Regulations, Hazards, Waste Management Strategies and Technologies for Value Recovery. *Waste Manage.* **2018**, *82*, 258−275.

(5) Diaz-Barriga-Fernandez, A. D.; Sañtibanez-Aguilar, J. E.; Radwan, N.; Nápoles-Rivera, F.; El-Halwagi, M. M.; Ponce-Ortega, J. M. Strategic Planning for Managing Municipal Solid Wastes with Consideration of Multiple Stakeholders. *ACS Sustainable Chem. Eng.* **2017**, *5*, 10744−10762.

(6) Scanlon, M. D.; Smirnov, E.; Stockmann, T. J.; Peljo, P. Gold Nanofilms at Liquid-Liquid Interfaces: An Emerging Platform for Redox Electrocatalysis, Nanoplasmonic Sensors, and Electrovariable Optics. *Chem. Rev.* **2018**, *118*, 3722−3751.

(7) Zhu, B.; Gong, S.; Cheng, W. Softening Gold for Elastronics. *Chem. Soc. Rev.* **2019**, *48*, 1668−1711.

(8) Alexander, C.; Litosh, S.; Alway, B.; Wiebe, J.; Li, S.; Saha, D.; Scott-Gray, N.; Gay, F.; Goenka, S. *GFMS Gold Survey* London 2019. http://solutions.refinitiv.com/MetalsResearch (accessed Mar 23, 2020).

(9) Rigoldi, A.; Trogu, E. F.; Marcheselli, G. C.; Artizzu, F.; Picone, N.; Colledani, M.; Deplano, P.; Serpe, A. Advances in Recovering Noble Metals from Waste Printed Circuit Boards (WPCBs). *ACS Sustainable Chem. Eng.* **2019**, *7*, 1308−1317.

(10) Nelson, J. J. M.; Schelter, E. J. Sustainable Inorganic Chemistry: Metal Separations for Recycling. *Inorg. Chem.* **2019**, *58*, 979−990.

(11) Rao, M. D.; Singh, K. K.; Morrison, C. A.; Love, J. B. Challenges and Opportunities in the Recovery of Gold from Electronic Waste. *RSC Adv.* **2020**, *10*, 4300−4309.

(12) Yue, C.; Sun, H.; Liu, W. J.; Guan, B.; Deng, X.; Zhang, X.; Yang, P. Environmentally Benign, Rapid, and Selective Extraction of Gold from Ores and Waste Electronic Materials. *Angew. Chem., Int. Ed.* **2017**, *56*, 9331−9335.

(13) Mon, M.; Ferrando-Soria, J.; Grancha, T.; Fortea-Perez, F. R.; Gascon, J.; Leyva-Perez, A.; Armentano, D.; Pardo, E. Selective Gold Recovery and Catalysis in a Highly Flexible Methionine-Decorated Metal-Organic Framework. *J. Am. Chem. Soc.* **2016**, *138*, 7864−7867.

(14) Yang, F.; Yan, Z.; Zhao, J.; Miao, S.; Wang, D.; Yang, P. Rapid Capture of Trace Precious Metals by Amyloid-Like Protein Membrane with High Adsorption Capacity and Selectivity. *J. Mater. Chem. A* **2020**, *8*, 3438−3449.

(15) Prochowicz, D.; Kornowicz, A.; Lewinski, J. Interactions of Native Cyclodextrins with Metal Ions and Inorganic Nanoparticles: Fertile Landscape for Chemistry and Materials Science. *Chem. Rev.* **2017**, *117*, 13461−13501.

(16) Pedersen, C. J. Cyclic Polyethers and Their Complexes with Metal Salts. *J. Am. Chem. Soc.* **1967**, *89*, 2495−2496.

(17) Pedersen, C. J. Cyclic Polyethers and Their Complexes with Metal Salts. *J. Am. Chem. Soc.* **1967**, *89*, 7017−7036.

(18) Homden, D. M.; Redshaw, C. The Use of Calixarenes in Metal-Based Catalysis. *Chem. Rev.* **2008**, *108*, 5086−5130.

(19) Chen, L.; Cai, Y.; Feng, W.; Yuan, L. Pillararenes as Macrocyclic Hosts: A Rising Star in Metal Ion Separation. *Chem. Commun.* **2019**, *55*, 7883−7898.

(20) Atwood, J. L.; Orr, G. W.; Hamada, F.; Vincent, R. L.; Bott, S. G.; Robinson, K. D. Calixarenes as Second-Sphere Ligands for Transition Metal Ions. Synthesis and Crystal Structure of $[(H_2O)_5Ni(NC_5H_5)]_2(Na)$[calix[4]arene sulfonate]·3.5 H_2O and $[(H_2O)_4Cu(NC_5H_5)_2]$-$(H_3O)_3$ [calix[4]arene sulfonate]·10 H_2O. *J. Inclusion Phenom. Mol. Recognit. Chem.* **1992**, *14*, 37−46.

(21) Alston, D. R.; Slawin, A. M. Z.; Stoddart, J. F.; Williams, D. J. Cyclodextrins as Second Sphere Ligands for Transition Metal Complexes—The X-ray Crystal Structure of $[Rh(cod)(NH_3)_2\cdot\alpha$-cyclodextrin$][PF_6]\cdot 6H_2O$. *Angew. Chem., Int. Ed. Engl.* **1985**, *24*, 786−787.

(22) Hua, B.; Shao, L.; Zhang, Z.; Liu, J.; Huang, F. Cooperative Silver Ion-Pair Recognition by Peralkylated Pillar[5]arenes. *J. Am. Chem. Soc.* **2019**, *141*, 15008−15012.

(23) Colquhoun, H. M.; Stoddart, J. F.; Williams, D. J. The Binding of Neutral Platinum Complexes by Crown Ethers. X-ray Crystal Structures of $[trans$-$PtCl_2(PMe_3)NH_3\cdot$dibenzo-18-crown-6] and $[\{trans$-$PtCl_2(PMe_3)NH_3\}_2\cdot$18-crown-6]. *J. Chem. Soc., Chem. Commun.* **1981**, 847−849.

(24) Ko, S. K.; Kim, S. K.; Share, A.; Lynch, V. M.; Park, J.; Namkung, W.; Van Rossom, W.; Busschaert, N.; Gale, P. A.; Sessler, J. L.; Shin, I. Synthetic Ion Transporters Can Induce Apoptosis by Facilitating Chloride Anion Transport Into Cells. *Nat. Chem.* **2014**, *6*, 885−892.

(25) Zahran, E. M.; Hua, Y.; Lee, S.; Flood, A. H.; Bachas, L. G. Ion-Selective Electrodes Based on a Pyridyl-Containing Triazolophane: Altering Halide Selectivity by Combining Dipole-Promoted Cooperativity with Hydrogen Bonding. *Anal. Chem.* **2011**, *83*, 3455−3461.

(26) Dutta, R.; Ghosh, P. Artificial Receptors for Nitrate: A Comprehensive Overview. *Chem. Commun.* **2015**, *51*, 9070−9084.

(27) Sheetz, E. G.; Qiao, B.; Pink, M.; Flood, A. H. Programmed Negative Allostery with Guest-Selected Rotamers Control Anion−Anion Complexes of Stackable Macrocycles. *J. Am. Chem. Soc.* **2018**, *140*, 7773−7777.

(28) Fatila, E. M.; Pink, M.; Twum, E. B.; Karty, J. A.; Flood, A. H. Phosphate-Phosphate Oligomerization Drives Higher Order Co-assemblies with Stacks of Cyanostar Macrocycles. *Chem. Sci.* **2018**, *9*, 2863−2872.

(29) Katayev, E. A.; Boev, N. V.; Khrustalev, V. N.; Ustynyuk, Y. A.; Tananaev, I. G.; Sessler, J. L. Bipyrrole- and Dipyrromethane-Based Amido-Imine Hybrid Macrocycles. New Receptors for Oxoanions. *J. Org. Chem.* **2007**, *72*, 2886−2896.

(30) Beer, P. D.; Gale, P. A. Anion Recognition and Sensing: The State of the Art and Future Perspectives. *Angew. Chem., Int. Ed.* **2001**, *40*, 486−516.

(31) Busschaert, N.; Caltagirone, C.; Van Rossom, W.; Gale, P. A. Applications of Supramolecular Anion Recognition. *Chem. Rev.* **2015**, *115*, 8038−8155.

(32) Molina, P.; Zapata, F.; Caballero, A. Anion Recognition Strategies Based on Combined Noncovalent Interactions. *Chem. Rev.* **2017**, *117*, 9907−9972.

(33) Liu, Z.; Frasconi, M.; Lei, J.; Brown, Z. J.; Zhu, Z.; Cao, D.; Iehl, J.; Liu, G.; Fahrenbach, A. C.; Botros, Y. Y.; Farha, O. K.; Hupp, J. T.; Mirkin, C. A.; Stoddart, J. F. Selective Isolation of Gold Facilitated by Second-Sphere Coordination with α-Cyclodextrin. *Nat. Commun.* **2013**, *4*, 1855.

(34) Liu, Z.; Samanta, A.; Lei, J.; Sun, J.; Wang, Y.; Stoddart, J. F. Cation-Dependent Gold Recovery with α-Cyclodextrin Facilitated by Second-Sphere Coordination. *J. Am. Chem. Soc.* **2016**, *138*, 11643−11653.

(35) Chen, L. X.; Liu, M.; Zhang, Y. Q.; Zhu, Q. J.; Liu, J. X.; Zhu, B. X.; Tao, Z. Outer Surface Interactions to Drive Cucurbit[8]uril-Based Supramolecular Frameworks: Possible Application in Gold Recovery. *Chem. Commun.* **2019**, *55*, 14271−14274.

(36) Lin, R. L.; Dong, Y. P.; Tang, M.; Liu, Z.; Tao, Z.; Liu, J. X. Selective Recovery and Detection of Gold with Cucurbit[n]urils (n = 5−7). *Inorg. Chem.* **2020**, *59*, 3850−3855.

(37) Freeman, W. A.; Mock, W. L.; Shih, N. Y. Cucurbituril. *J. Am. Chem. Soc.* **1981**, *103*, 7367−7368.

(38) Lagona, J.; Mukhopadhyay, P.; Chakrabarti, S.; Isaacs, L. The Cucurbit[n]uril Family. *Angew. Chem., Int. Ed.* **2005**, *44*, 4844−4870.

https://dx.doi.org/10.1021/acsami.0c09673
ACS Appl. Mater. Interfaces XXXX, XXX, XXX−XXX

(39) Barrow, S. J.; Kasera, S.; Rowland, M. J.; del Barrio, J.; Scherman, O. A. Cucurbituril-Based Molecular Recognition. *Chem. Rev.* **2015**, *115*, 12320−12406.
(40) Jeon, Y.-M.; Kim, J.; Whang, D.; Kim, K. Molecular Container Assembly Capable of Controlling Binding and Release of Its Guest Molecules: Reversible Encapsulation of Organic Molecules in Sodium Ion Complexed Cucurbituril. *J. Am. Chem. Soc.* **1996**, *118*, 9790−9791.
(41) Heo, J.; Kim, S.-Y.; Whang, D.; Kim, K. Shape-Induced, Hexagonal, Open Frameworks: Rubidium Ion Complexed Cucurbituril. *Angew. Chem., Int. Ed.* **1999**, *38*, 641−643.
(42) Gerasko, O. A.; Mainicheva, E. A.; Naumova, M. I.; Neumaier, M.; Kappes, M. M.; Lebedkin, S.; Fenske, D.; Fedin, V. P. Sandwich-Type Tetranuclear Lanthanide Complexes with Cucurbit[6]uril: From Molecular Compounds to Coordination Polymers. *Inorg. Chem.* **2008**, *47*, 8869−8880.
(43) Thuery, P. Uranyl-Lanthanide Heterometallic Complexes with Cucurbit[6]uril and Perrhenate Ligands. *Inorg. Chem.* **2009**, *48*, 825−827.
(44) Ghale, G.; Nau, W. M. Dynamically Analyte-Responsive Macrocyclic Host-Fluorophore Systems. *Acc. Chem. Res.* **2014**, *47*, 2150−2159.
(45) Lim, S.; Kim, H.; Selvapalam, N.; Kim, K. J.; Cho, S. J.; Seo, G.; Kim, K. Cucurbit[6]uril: Organic Molecular Porous Material with Permanent Porosity, Exceptional Stability, and Acetylene Sorption Properties. *Angew. Chem., Int. Ed.* **2008**, *47*, 3352−3355.
(46) Kim, H.; Kim, Y.; Yoon, M.; Lim, S.; Park, S. M.; Seo, G.; Kim, K. Highly Selective Carbon Dioxide Sorption in an Organic Molecular Porous Material. *J. Am. Chem. Soc.* **2010**, *132*, 12200−12202.
(47) Lee, H. K.; Park, K. M.; Jeon, Y. J.; Kim, D.; Oh, D. H.; Kim, H. S.; Park, C. K.; Kim, K. Vesicle Formed by Amphiphilc Cucurbit[6]-uril: Versatile, Noncovalent Modification of the Vesicle Surface, and Multivalent Binding of Sugar-Decorated Vesicles to Lectin. *J. Am. Chem. Soc.* **2005**, *127*, 5006−5007.
(48) Wu, X.; Zhang, Y.-M.; Liu, Y. Nanosupramolecular Assembly of Amphiphilic Guest Mediated by Cucurbituril for Doxorubicin Delivery. *RSC Adv.* **2016**, *6*, 99729−99734.
(49) Kim, K.; Jeon, W. S.; Kang, J. K.; Lee, J. W.; Jon, S. Y.; Kim, T.; Kim, K. A Pseudorotaxane on Gold: Formation of Self-Assembled Monolayers, Reversible Dethreading and Rethreading of the Ring, and Ion-Gating Behavior. *Angew. Chem., Int. Ed.* **2003**, *42*, 2293−2296.
(50) Park, K. M.; Yang, J. A.; Jung, H.; Yeom, J.; Park, J. S.; Park, K. H.; Hoffman, A. S.; Hahn, S. K.; Kim, K. In Situ Supramolecular Assembly and Modular Modification of Hyaluronic Acid Hydrogels for 3D Cellular Engineering. *ACS Nano* **2012**, *6*, 2960−2968.
(51) Ke, C.; Smaldone, R. A.; Kikuchi, T.; Li, H.; Davis, A. P.; Stoddart, J. F. Quantitative Emergence of Hetero[4]rotaxanes by Template-Directed Click Chemistry. *Angew. Chem., Int. Ed.* **2013**, *52*, 381−387.
(52) Finbloom, J. A.; Han, K.; Slack, C. C.; Furst, A. L.; Francis, M. B. Cucurbit[6]uril-Promoted Click Chemistry for Protein Modification. *J. Am. Chem. Soc.* **2017**, *139*, 9691−9697.
(53) Lin, R.-G.; Long, L.-S.; Huang, R.-B.; Zheng, L.-S. Directing Role of Hydrophobic−Hydrophobic and Hydrophilic−Hydrophilic Interactions in the Self-Assembly of Calixarenes / Cucurbiturils-Based Architectures. *Cryst. Growth & Des.* **2008**, *8*, 791−794.
(54) Ni, X. L.; Xiao, X.; Cong, H.; Zhu, Q. J.; Xue, S. F.; Tao, Z. Self-Assemblies Based on the "Outer-Surface Interactions" of Cucurbit[*n*]urils: New Opportunities for Supramolecular Architectures and Materials. *Acc. Chem. Res.* **2014**, *47*, 1386−1395.
(55) Freeman, W. A. Structures of the *p*-Xylylenediammonium Chloride and Calcium Hydrogensulfate Adducts of the Cavitand 'Cucurbituril', $C_{36}H_{36}N_{24}O_{12}$. *Acta Crystallogr., Sect. B: Struct. Sci.* **1984**, *40*, 382−387.
(56) Bisson, A. P.; Lynch, V. M.; Monahan, M.-K. C.; Anslyn, E. V. Recognition of Anions through NH−π Hydrogen Bonds in a Bicyclic Cyclophane—Selectivity for Nitrate. *Angew. Chem., Int. Ed. Engl.* **1997**, *36*, 2340−2342.
(57) Lopez, N.; Graham, D. J.; McGuire, R., Jr.; Alliger, G. E.; Shao-Horn, Y.; Cummins, C. C.; Nocera, D. G. Reversible Reduction of Oxygen to Peroxide Facilitated by Molecular Recognition. *Science* **2012**, *335*, 450−453.
(58) Liu, Y.; Zhao, W.; Chen, C. H.; Flood, A. H. Chloride Capture Using a C−H Hydrogen-Bonding Cage. *Science* **2019**, *365*, 159−161.
(59) Valkenier, H.; Akrawi, O.; Jurček, P.; Sleziaková, K.; Lízal, T.; Bartik, K.; Šindelář, V. Fluorinated Bambusurils as Highly Effective and Selective Transmembrane Cl^-/HCO_3^- Antiporters. *Chem* **2019**, *5*, 429−444.
(60) Ni, X. L.; Xiao, X.; Cong, H.; Liang, L. L.; Cheng, K.; Cheng, X. J.; Ji, N. N.; Zhu, Q. J.; Xue, S. F.; Tao, Z. Cucurbit[*n*]uril-Based Coordination Chemistry: From Simple Coordination Complexes to Novel Poly-Dimensional Coordination Polymers. *Chem. Soc. Rev.* **2013**, *42*, 948−508.
(61) Wu, H.; Chen, Y.; Dai, X.; Li, P.; Stoddart, J. F.; Liu, Y. In Situ Photoconversion of Multicolor Luminescence and Pure White Light Emission Based on Carbon Dot-Supported Supramolecular Assembly. *J. Am. Chem. Soc.* **2019**, *141*, 6583−6591.
(62) Johnson, N. J.; Korinek, A.; Dong, C.; van Veggel, F. C. Self-Focusing by Ostwald Ripening: A Strategy for Layer-by-Layer Epitaxial Growth on Upconverting Nanocrystals. *J. Am. Chem. Soc.* **2012**, *134*, 11068−11071.
(63) Ouyang, R.; Liu, J. X.; Li, W. X. Atomistic Theory of Ostwald Ripening and Disintegration of Supported Metal Particles under Reaction Conditions. *J. Am. Chem. Soc.* **2013**, *135*, 1760−1771.
(64) Bardelang, D.; Udachin, K. A.; Leek, D. M.; Margeson, J. C.; Chan, G.; Ratcliffe, C. I.; Ripmeester, J. A. Cucurbit[*n*]urils (*n* = 5−8): A Comprehensive Solid State Study. *Cryst. Growth & Des.* **2011**, *11*, 5598−5614.
(65) Pettman, R. B.; Arnold, D. F. *Recovery of Precious and Rare Earth Metals Using Cyclodextrin. International Publication Number* WO 2017/158561 A1, Sept 21, 2017.
(66) Xing, W. D.; Lee, M. S. Leaching of Gold and Silver from Anode Slime with a Mixture of Hydrochloric Acid and Oxidizing Agents. *Geosyst. Eng.* **2017**, *20*, 216−223.

https://dx.doi.org/10.1021/acsami.0c09673
ACS Appl. Mater. Interfaces XXXX, XXX, XXX−XXX